Solar RRL
www.solar-rrl.com

Interface Engineering via Sputtered Oxygenated CdS:O Window Layer for Highly Efficient Sb_2Se_3 Thin-Film Solar Cells with Efficiency Above 7%

Liping Guo, Baiyu Zhang, Smriti Ranjit, Jacob Wall, Swapnil Saurav, Adam J. Hauser, Guozhong Xing, Lin Li, Xiaofeng Qian, and Feng Yan**

Antimony chalcogenide Sb_2Se_3 is an emerging photovoltaic absorber due to its appropriate bandgap (≈1.1 eV), high absorption coefficient (>10^5 cm^{-1}), suitable p-type conductivity, low toxicity, earth abundance, and excellent stability. However, the stringent growth condition and low photovoltage limit its power conversion efficiency (PCE). Herein, via a combined theoretical and experimental study, interface engineering via an oxygenated cadmium sulfide (CdS) window layer (CdS:O) is found to be an effective approach to improve the device performance of CdS:O/Sb_2Se_3 solar cells. The sputtered oxygenated CdS:O window layer can be used to replace conventional chemical-bath-deposited CdS window layer in the Sb_2Se_3 devices. The best PCE of 7.01% is demonstrated in the superstrate configuration of fluorine-doped SnO_2/CdS:O/Sb_2Se_3/graphite with a high open-circuit voltage of 0.432 V, where Sb_2Se_3 is fabricated using the close space sublimation technique. The interfacial diffusion between Sb_2Se_3 and sputtered CdS:O is significantly suppressed by introducing oxygen at the interface, which prevents Cd diffusion and the formation of Cd interstitials. Combined device physics characterizations and theoretical calculations reveal that oxygen in the CdS:O/Sb_2Se_3 interface can increase depletion region, built-in voltage, and reduce interfacial recombination. These findings provide the guidance to optimize quasi-one-dimensional non-cubic earth-abundant chalcogenide photovoltaic devices through interface engineering.

1. Introduction

Efficient, stable, and earth-abundant thin-film photovoltaic materials are highly desired for harvesting solar energy and providing renewable and affordable energy.[1] Recently, low-cost non-cubic Sb_2Se_3 has become a promising photovoltaic absorber candidate with orthorhombic structure (space group Pbnm).[2] It possesses unique quasi-one-dimensional ribbons, i.e., $(Sb_4Se_6)_n$, featuring anisotropic and effective photoexcited carrier transport.[3,4] The desired optical bandgap (≈1.1 eV) and superior absorption coefficient (>10^5 cm^{-1}) endow Sb_2Se_3 with great potential for applications in thin-film solar cells.[5] The power conversion efficiency (PCE) of superstrated FTO/CdS/Sb_2Se_3 thin-film solar cells was boosted close to ≈7.6%, and substrated Mo/$MoSe_2$/Sb_2Se_3/CdS solar cells have achieved 9.2% PCE.[3,6] Several techniques have been used to grow high-quality Sb_2Se_3 absorber layer, including close space sublimation (CSS),[7,8] vapor transport deposition (VTD),[3] and rapid thermal evaporation (RTE).[2,4,9,10] The quasi-one-dimensional $(Sb_4Se_6)_n$ ribbon orientation is significantly impacted by the film deposition parameters, such as substrate temperature, source temperature, and the post-sensitization of the deposited film.[2,11–13] Remarkably, a wide range of the window layer materials (e.g., ZnO, TiO_2, and CdS) have been used to tune the ribbon orientation and suspend the device degradation.[4,13,14] However, the champion device performance is still far from its theoretical PCE limit (≈31%).[5] The photovoltaic device performance is severely limited by the low open-circuit

L. Guo, J. Wall, S. Saurav, Dr. L. Li, Dr. F. Yan
Department of Metallurgical and Materials Engineering
The University of Alabama
Tuscaloosa, AL 35487, USA
E-mail: fyan@eng.ua.edu

B. Zhang, Dr. X. Qian
Department of Materials Science and Engineering
Texas A&M University
College Station, TX 77843, USA
E-mail: feng@tamu.edu

The ORCID identification number(s) for the author(s) of this article can be found under https://doi.org/10.1002/solr.201900225.

DOI: 10.1002/solr.201900225

S. Ranjit, Dr. A. J. Hauser
Department of Physics and Astronomy
The University of Alabama
Tuscaloosa, AL 35487, USA

Dr. G. Xing
United Microelect. Corp. Ltd.
Singapore 519528, Singapore

voltage (V_{OC}) of ≈0.4 V in contrast to its bandgap of 1.1 eV due to abundant deep defects,[15] although the short-circuit current density (J_{SC}) was improved to ≈30 mA cm^{-2}.[16] Given the well-known Cu(In/Ga)Se (CIGS) (≈22% PCE) technology with similar bandgap (≈1.1 eV) and its V_{OC} record of ≈0.744 V, it is worth developing effective approaches to lift the V_{OC} in Sb_2Se_3 solar cells.[17]

Sputtered oxygenated CdS (CdS:O) window layer can improve the V_{OC} in CdTe and other chalcogenide solar cells (such as Cu_2BaSnS_4) due to its high resistivity and transparency.[18–21] The CdS:O window layer is composed by CdS and $CdSO_x$ with a wide bandgap range (2.4–3.7 eV), which can be achieved by engineering oxygen composition during the reactive sputtering deposition.[20] Moreover, the high resistivity of CdS:O window layers can passivate the absorber/CdS:O interface and suspend the interface recombination.[20] Thus, both V_{OC} and J_{SC} can be improved by introducing sputtered oxygenated CdS:O to CdTe devices.[22] To date, the most widely used window layer for high-efficiency Sb_2Se_3 cells is the chemical bath deposited (CBD) CdS window layer.[3,6,7] Therefore, it is necessary to conduct an systematic investigation on the effect of sputtered oxygenated CdS:O window layer on the Sb_2Se_3 devices. Meanwhile, the presence of oxygen in CdS window layers can optimize the interdiffusion at the CdS/CdTe interface.[23] The existence of oxygen in CdTe solar cells can increase the acceptor concentration and lifetime.[24] Thus, the oxygen in CdS and CdTe can improve the CdS/CdTe device performance. It has also been reported that introducing oxygen during the Sb_2Se_3 deposition could passivate interface defects and lead to enhanced device performance.[11] However, the impact of oxygen in the sputtered oxygenated CdS:O window layer on the Sb_2Se_3 device performance is unclear.

Here, we present our first-principles theoretical calculations and experimental studies to understand the role of interfacial oxygen in the CdS:O/Sb_2Se_3 heterostructure. Our first-principles calculations indicate the interdiffusion mechanism and defect chemistry associated with the oxygenated CdS:O window layer–based Sb_2Se_3 solar cells. Oxygen has a higher diffusion barrier across $(Sb_4Se_6)_n$ ribbons (i.e., perpendicular to the ribbon direction) than that along with the ribbons inside the van der Waals (vdW) gap. Controlling oxygen content in the interfacial area of CdS:O/Sb_2Se_3 can effectively passivate the vdW gap of Sb_2Se_3, thereby blocking the Cd diffusion into Sb_2Se_3 to form n-type Cd_i interstitials. Our theoretical study suggests that higher V_{OC} can be achieved in the Sb_2Se_3 thin-film solar cells with interface engineering. Following the theoretical prediction, we propose to replace the conventional CBD CdS layer by sputtered oxygenated CdS:O window layer to passivate the interface between the window layer and Sb_2Se_3. By systematic tuning of oxygen concentration in the sputtered oxygenated CdS:O layer, we achieved the highest V_{OC} (≈0.432 V), J_{SC} (≈29.9 mA cm^{-2}), and PCE (≈7.01%) in the CSS-grown Sb_2Se_3 devices with the superstrate F:SnO_2/CdS:O/ Sb_2Se_3/graphite/Ag device architecture. The reactively sputtered oxygenated CdS:O window layer effectively enhances the bandgap of CdS:O and tailors the $(Sb_4Se_{6)n}$ ribbons to (211)-textured orientation. The grain size of Sb_2Se_3 grown on the sputtered CdS:O is larger than that on CBD CdS, suggesting that the oxygen in the CdS:O can also impact the Sb_2Se_3 growth. The interfacial element distribution analysis indicates that the interfacial oxygen can suppress the CdS/Sb_2Se_3 interdiffusion, which prevents the Cd interstitial formation in Sb_2Se_3 absorber layer. In addition, the device physics analysis demonstrated that the increased V_{OC} stems from the improved built-in voltage, and the improved J_{SC} comes from the thicker depletion region and the reduced interfacial recombination in the CdS:O/Sb_2Se_3 device. This study of extrinsic point defects based on first-principles density functional theory (DFT) further proves that oxygen-associated defects, substitutional defects (O_{Sb}) and (O_{Se}) and interstitial defect (O_i), hardly become n-type. However, Cd interstitial (Cd_i) is a donor defect; therefore to reduce its concentration, the Se-rich condition is desired. These theoretical and experimental findings demonstrate that interface engineering is an effective approach to improve the device performance of Sb_2Se_3 thin-film solar cells, which can be used to break the photovoltage limit in Sb_2Se_3 solar cells.

2. Results and Discussion

To elucidate the role of oxygen in the interface between CdS and Sb_2Se_3, we first investigate the diffusion behavior using first-principles DFT calculations. Two diffusion pathways were considered in the calculations for both Cd and O atoms (**Figure 1**). One diffusion pathway is along with the $(Sb_4Se_6)_n$ ribbons as shown in Figure 1a,b for Cd and O, respectively. The other diffusion pathway is across the $(Sb_4Se_6)_n$ ribbons, as shown in Figure 1d,e. The calculated diffusion energy barriers are shown in Figure 1c,f for the diffusion across and along with ribbons, respectively. As shown in **Table 1**, the diffusion barrier of Cd along ribbons is ≈0.6 eV, whereas Cd diffusion across ribbons is about 0.8 eV. The diffusion barrier of O across ribbons is ≈1.7 eV, which is much higher than ≈1 eV for O diffusion along with ribbons. In both cases, Cd has a lower diffusion barrier than that of O, suggesting that Cd diffusion is relatively faster than O. It may be related to their degraded stabilities due to diffusion.[11] The high diffusion energy barriers of oxygen suggest that oxygenating the CdS/Sb_2Se_3 interface may fill the vdW gaps and block Cd diffusion.

In experiments, Cd and S could be unintentionally introduced from the buffer layer CdS to the absorber layer Sb_2Se_3. We, therefore, study the formation energies of three potential impurity elements in Sb_2Se_3, namely O, Cd, and S, associated point defects, including substitution and interstitial defect types. Although Sb_2Se_3 is a binary semiconductor, it is structurally multinary due to its low symmetry. The unit cell of antimony selenide has a space group of Pbnm, consisting of two quasi-one-dimensional Sb_4Se_6 chains, i.e., 8 Sb atoms and 12 Se atoms. Among the total 20 atoms per unit cell, there are two Sb sites and three Se sites which are symmetrically inequivalent (labeled in Figure 1e), resulting in the structurally multinary nature with complicated defect properties as recently pointed out by Huang et al.[15] Thus, two extreme conditions were considered together with multiple inequivalent Sb and Se sites: 1) Se-rich condition and 2) Se-poor condition, as shown in **Figure 2**a,b, respectively. Since the intrinsic defects in the Sb_2Se_3 absorbers have been investigated,[15,25] we focus on nine types of extrinsic defects, including three interstitial defects Cd_i, S_i, and O_i and six

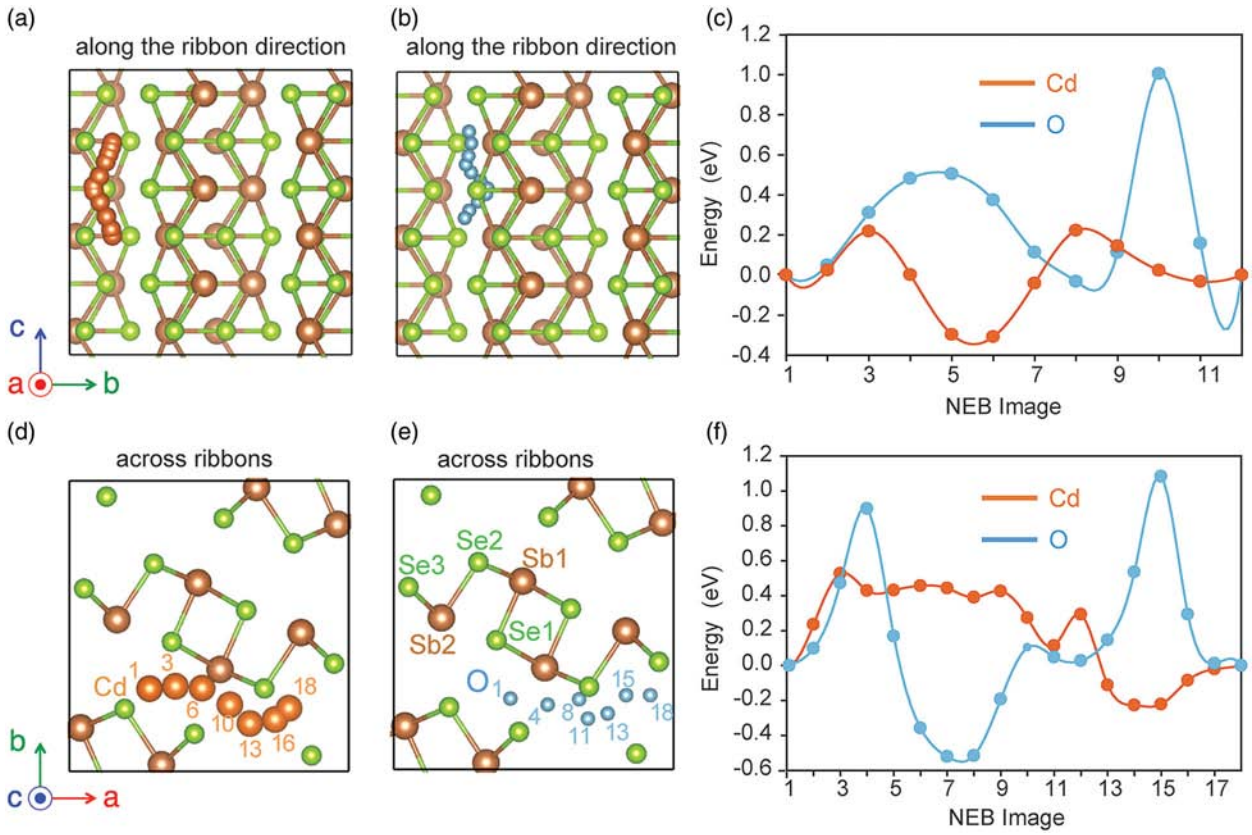

Figure 1. Calculated Cd and O diffusion pathways and energy barriers in Sb_2Se_3: a) Cd and b) O diffusion along with ribbons; c) diffusion energy barrier along with ribbons; d) Cd and e) O diffusion across ribbons; and f) diffusion energy barrier across ribbons. Symmetrically inequivalent Sb and Se sites are labeled in e) including Sb1, Sb2, Se1, Se2, and Se3.

Table 1. Diffusion energy barrier for Cd and O across and along with the $(Sb_4Se_6)_n$ ribbons.

	Energy barrier [eV]	
Diffusion element	Across ribbons	Along with ribbons
Cd	0.8	0.6
O	1.7	1.0

substitutional defects Cd_{Se}, Cd_{Sb}, S_{Se}, S_{Sb}, O_{Se}, and O_{Sb}. As mentioned earlier, among the substitutional defects, there are three different Se sites and two different Sb sites, resulting in X_{Se1}, X_{Se2}, X_{Se3}, X_{Sb1}, and X_{Sb1}, where X is Cd, S, or O. In general, the defect formation energy diagrams (Figure 2a,b) and the transition level diagram (Figure 2c) show that the substitutional defects at the symmetrically inequivalent sites in Sb_2Se_3 lead to dispersed transition levels and defect formation energies, especially in the case of S_{Sb1} and S_{Sb2}. This is similar to the case of intrinsic point defects reported by Huang et al.[15] Furthermore, under the Se-rich condition (Figure 2a), O_{Se}, S_{Se}, O_i, and Cd_{Sb} have relatively low formation energies below 1.0 eV. For the Cd-related defects (e.g., Cd_i, Cd_{Se}, and Cd_{Sb}), the donor defects Cd_i and Cd_{Se} have relatively high defect formation energy compared with that of the Cd_{Sb} substitutional defect (Figure 2a), whereas the Cd_{Sb} defect is a shallow acceptor defect with transition level of $\epsilon(1-/0) = 0.1$ eV above the valence band maximum (VBM) (Figure 2c). It also shows that Cd_{Sb} could improve the p-type conduction of the Sb_2Se_3. However, it was experimentally reported that the Cd atoms diffusing into the Sb_2Se_3 and forming Cd_i could produce a buried homojunction and lead to n-type conduction in Sb_2Se_3.[26] Indeed, our results reveal that, when Cd stays in the vdW gap between $(Sb_4Se_6)_n$ ribbons as Cd_i defect, it becomes a shallow donor with transition level $\epsilon(2+/0)$ located at ≈0.7 eV (relatively close to conduction band minimum [CBM], Figure 2c), thereby causing n-type conduction. For the S-induced point defects (i.e., S_i, S_{Sb}, and S_{Se}), both S_i and S_{Sb} have formation energy above 1 eV, but the S_{Se} substitutional defect has almost zero defect formation energy, suggesting that S could randomly replace Se in the Sb_2Se_3. This low S_{Se} substitutional defect formation energy can also be explained by the complete solid solution of ternary $Sb_2(S, Se)_3$.[27] Finally, among three O-related point defects (i.e., O_i, O_{Se}, and O_{Sb}), O_{Se} has the lowest formation energy, indicating that O tends to replace Se. O_i interstitial defect has relatively low formation energy, implying that it is likely that oxygen will be located at the vdW gaps between the $(Sb_4Se_6)_n$ ribbons. Under the Se-poor condition, the S_{Se} defects have the lowest defect formation energy, and the Cd_i defects are also easy to form due to its low formation energy, whereas the other defects associated with CdS:O window

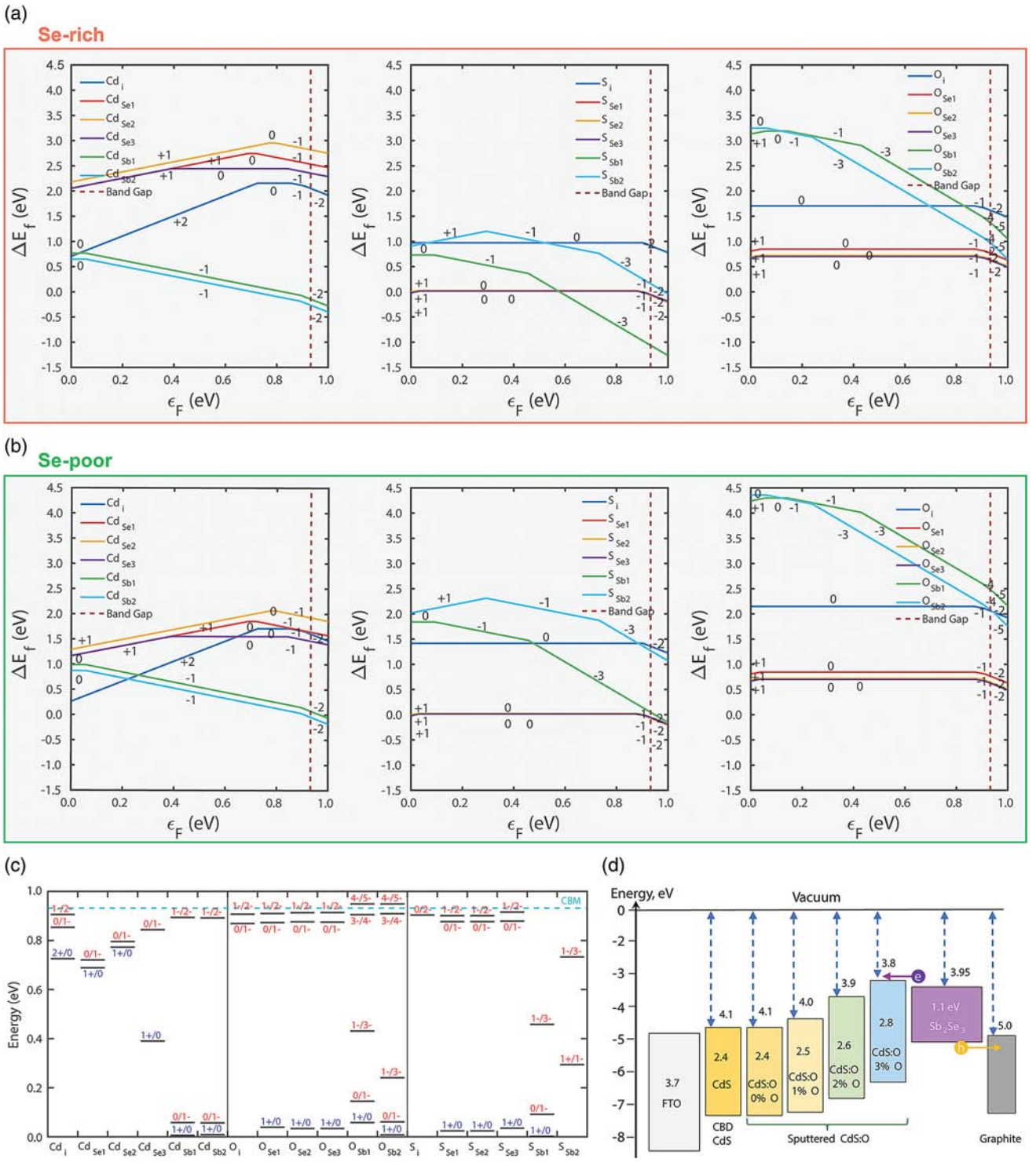

Figure 2. Defect analysis of Sb_2Se_3 thin-film solar cells and interface engineering with CdS:O window layer. a,b) the calculated formation energy of point defects as a function of Fermi level for Sb-rich and Se-poor condition, respectively; c) transition levels of potential extrinsic point defects in the Sb_2Se_3 absorbers; and d) energy band diagram for interfacial engineering with sputtered oxygenated CdS:O at 0%, 1%, 2%, and 3% oxygen partial pressure.

layers have higher formation energy (above 1 eV). This observation agrees with the reported data that Sb_2Se_3 under the Se-poor condition has poor conductivity and low device performance in general. To improve the device performance, it is necessary to perform post-selenization for the deposited films to suppress the donor defects like Cd_i at the Se-poor condition.[25]

The above first-principles electronic structure calculations indicate that introducing oxygen at the CdS/Sb_2Se_3 interface can form stable O_i due to relatively low defect formation energy, high O diffusion barrier, and filled the vdW gaps between Sb_2Se_3 ribbons with benign transition levels. The latter can effectively reduce Cd_i induced n-type conduction. More specifically, the oxygenated sputtered CdS:O window layer could also provide oxygen to occupy the Se sites (O_{Se}) in the Sb_2Se_3, where O_{Se} has the lowest formation energy without generating detrimental charge defect (Figure 2a). Partial oxygen can also enter into the vdW gaps between the $(Sb_4Se_6)_n$ ribbons, which will block and suppress the Cd diffusion, thereby preventing the formation of Cd_i defect in the bulk of Sb_2Se_3. In fact, the oxygen diffusion barrier across/along ribbons is high (≈1.7/1.0 eV), as shown in Figure 1. Therefore, the oxygen will accumulate at the CdS:O/Sb_2Se_3 interface. Considering that Cd_i exhibits a shallow n-type transition level, which is ≈0.2 eV from CBM (Figure 2c), the suppressed Cd_i formation will reduce the n-type buried heterostructure. Thus, we can expect the enhanced device performance in oxygenated $CdS:O/Sb_2Se_3$ devices by tuning the interfacial oxygen composition. The schematic energy band diagram is shown in Figure 2d.

In light of the above theoretical insights, we deposit Sb_2Se_3 absorbers on sputtered oxygenated CdS:O films at slightly Se-rich condition during the CSS process and investigate the impact of oxygen content in the Sb_2Se_3 solar absorber material.[8] The sputtered oxygenated CdS:O window layers were characterized using both the X-ray diffraction (XRD) and X-ray photoelectron spectroscopy (XPS). The sputtered pure CdS without oxygen shows a hexagonal crystalline structure, whereas the oxygenated CdS:O layers show nanocrystalline structure with reduced grain size (Figure S1c,d, Supporting Information). Meanwhile, the XPS measurements on the sputtered oxygenated CdS layers indicate that the $CdSO_3$ and $CdSO_4$ components are formed in the sputtered oxygenated CdS:O (Figure S2, Supporting Information). **Figure 3**a shows the UV–vis absorption spectra of the sputtered oxygenated CdS:O films. The inset shows the optical image of CdS:O films with $O_2/(O_2 + Ar)$ of 0%, 1%, 2%, and 3%. The transmittance increases with increasing oxygen partial pressure. The as-deposited CdS, i.e., $O_2/(O_2 + Ar)$ ≈0%, shows a strong absorption at the blue range (<500 nm), which is similar to the CBD CdS (Figure S1, Supporting Information). The bandgap, indicated by the dashed line in Figure 3b, increases from 2.4 to 2.85 eV as more oxygen was introduced in the

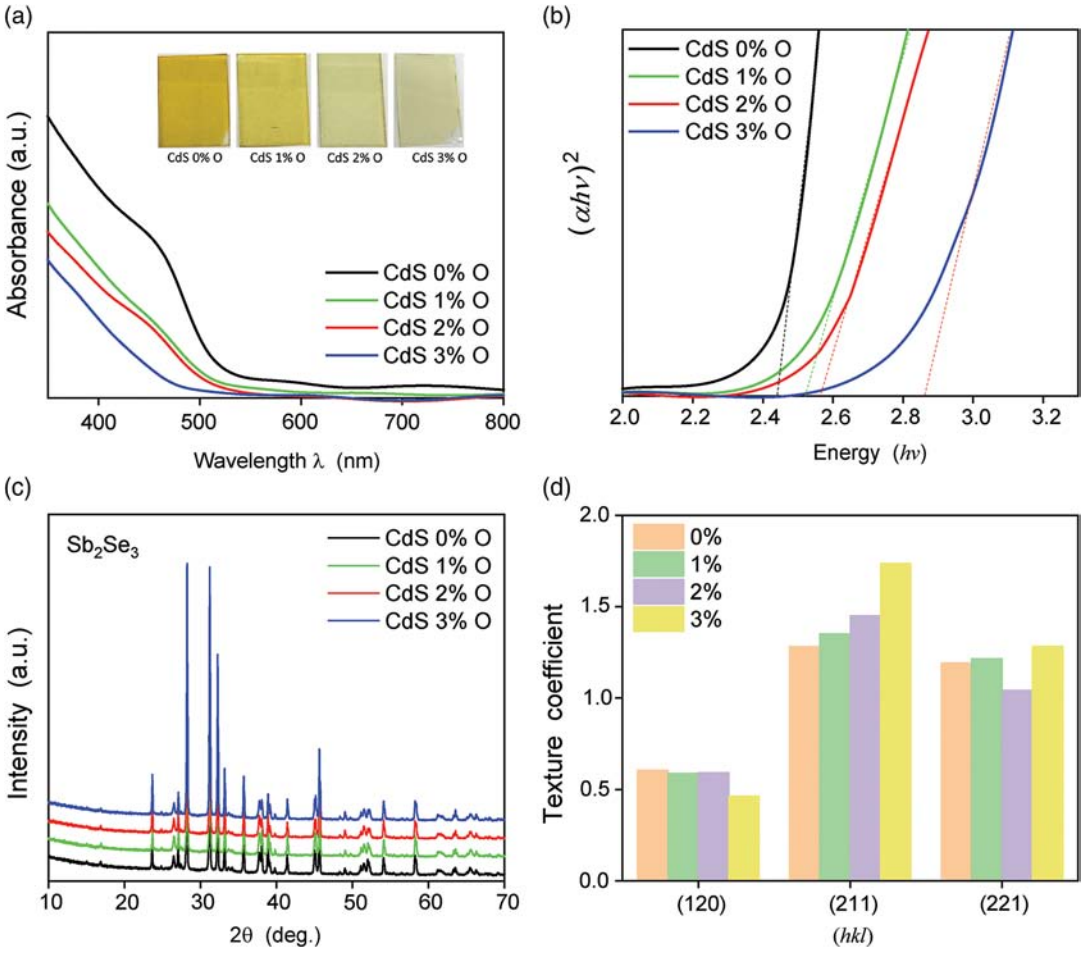

Figure 3. a) UV–vis absorbance spectra for the oxygenated CdS, and the inset shows the oxygenated CdS:O samples with increasing oxygen partial pressure of 0%, 1%, 2%, and 3% O_2 during deposition; b) absorption coefficient extracted from the optical transmittance; c) XRD pattern of the CSS-deposited Sb_2Se_3 films; and d) TC determined from the Sb_2Se_3 films grown on oxygenated CdS:O window layer.

CdS:O layer during sputtering, in agreement with previous studies.[19] The increased bandgap was attributed to the formation of the Cd sulfate ($CdSO_4$) and sulfur compounds ($CdSO_x$) with wide bandgaps.[20] Figure 3c shows the XRD pattern of CdS:O/Sb_2Se_3 films deposited at identical CSS conditions by controlling the oxygenated CdS:O window layers only. The Sb_2Se_3 films show orthorhombic structure (space group Pbnm) in agreement with the PDF-0015-0861. To inspect the texture effect by the CdS:O window layer, the texture coefficients (TCs) were calculated, as shown in Figure 3d. It was observed that the TCs gradually change to (211)-orientation, whereas the (120)-orientation was reduced when more oxygen was introduced into CdS:O. The increased TCs of (211)-textured orientation with increasing oxygen in the oxygenated sputtered CdS:O can be associated with the decreased CdS:O grain size and crystallinity, as shown in the atomic force microscopy (AFM) topography (Figure S1c, Supporting Information). It is known that (211)-textured orientation can benefit the device performance with lower series resistivity.[2] Figure S2a,b, Supporting Information, shows the optical absorption and extracted bandgap for a representative CdS:O/Sb_2Se_3 film grown at 2% oxygen partial pressure. The direct and indirect bandgaps are 1.21 and 1.16 eV, respectively, consistent with the previous study.[8]

Figure 4 shows the statistic distribution of Sb_2Se_3 device parameters measured under air mass (AM) 1.5G. It demonstrates that V_{OC}, J_{SC}, $R_{SH,}$ and FF improve with the increased oxygen in CdS:O until 2% O_2. The corresponding PCEs are also significantly elevated, and the series resistance R_S was decreased accordingly. The improved V_{OC} mainly originates from the reduced carrier recombination at the CdS:O/Sb_2Se_3 heterostructure interface, i.e., the recombination of the holes from Sb_2Se_3 and the electrons from CdS:O layers due to the band misalignment and lattice mismatch between CdS:O and Sb_2Se_3. The formation of highly resistive $CdSO_x$ ($x = 3$ or 4) can passivate the CdS:O/Sb_2Se_3 interface to prevent the carrier recombination. The highest V_{OC} of ≈0.432 V can be achieved by depositing CdS:O at 2% oxygen partial pressure. However, as the oxygen partial pressure further increases to ≈3%, the series resistance R_S increases significantly (Figure 4d), suggesting that more CdS was converted into insulating $CdSO_4$ with increasing the oxygen content, which prevents the electron transport in the window layer. By increasing oxygen partial pressure from 0% to 2%, the mean J_{SC} was dramatically increased from ≈25.5 to 29 mA cm^{-2} (Figure 4c), indicating more photons were absorbed in the short-wavelength exciting electron-hole pairs. The improved J_{SC} is associated with the enhanced transparency of CdS:O, which was also confirmed by external quantum efficiency (EQE) measurment shown in **Figure 5**b. However, with excess oxygen (>2%) introduced into the CdS:O layer, the J_{SC} decreases due to the spike-like (type-I) conduction band alignment between CdS:O and Sb_2Se_3 (Figure 2d). In other words, the CBM of CdS:O (3% O) is higher than that of Sb_2Se_3. This CBM offset will reduce electron transport from Sb_2Se_3 to the front FTO even if more light is absorbed in the absorber layer. Here, the sharply increased FFs are attributed to the reduced series resistivity, R_S, as shown in Figure 4e. The obtained optimal sputtering oxygen partial pressure for CdS:O is ≈2%, which agrees with the observation of CdS:O used for CdTe devices in various groups.[21,28,29]

Figure 5a shows the *J–V* curves of champion Sb_2Se_3 cells with the CdS:O window layers sputtered with varying oxygen partial pressure at ambient temperature. The corresponding cell parameters are listed in **Table 2**. The best CdS:O/Sb_2Se_3 device was obtained using the window layer sputtered at 2% oxygen partial pressure, where a PCE of 7.01%, a V_{OC} of 0.432 V, an FF of 54%, and a J_{SC} of ≈29.87 mA cm^{-2} were achieved with CdS:O bandgap of ≈2.6 eV. Figure 5b shows that the EQE curves of these CdS:O/Sb_2Se_3 devices, where the blue-shift of EQE at short wavelength is originated from the increased bandgap of

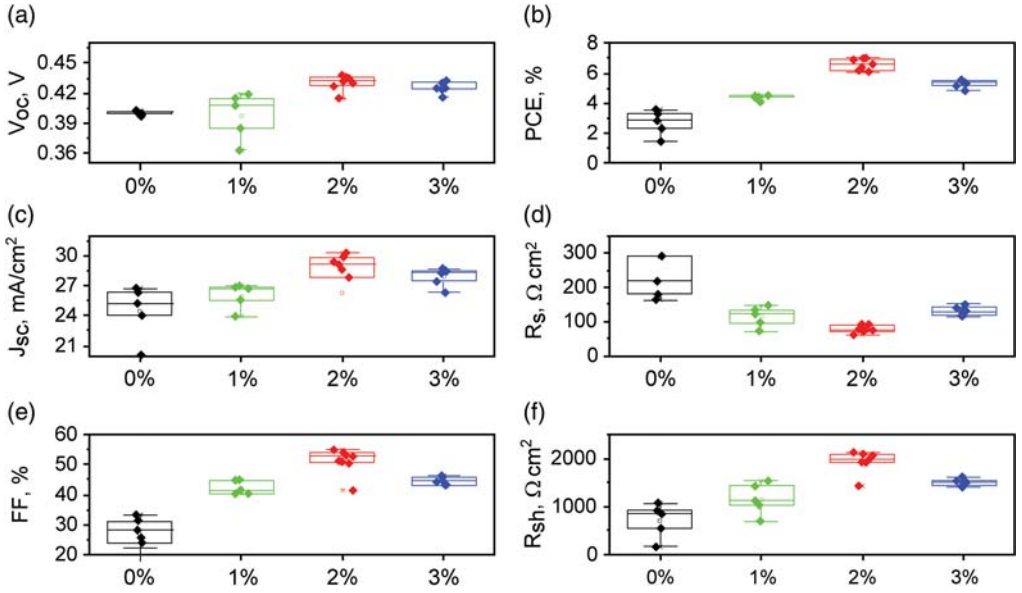

Figure 4. Statistic distribution of Sb_2Se_3 device performance parameters with the FTO/CdS:O/Sb_2Se_3/graphite/Ag architecture. The sputtered oxygenated CdS:O window layers were grown in the $O_2/(Ar + O_2)$ ratio at 0%, 1%, 2%, and 3% at ambient temperature. a) Open-circuit voltage (V_{OC}), b) PCE, c) short-circuit photocurrent (J_{SC}), d) series resistance (R_S), e) fill factor (FF), and f) shunt resistance (R_{SH}).

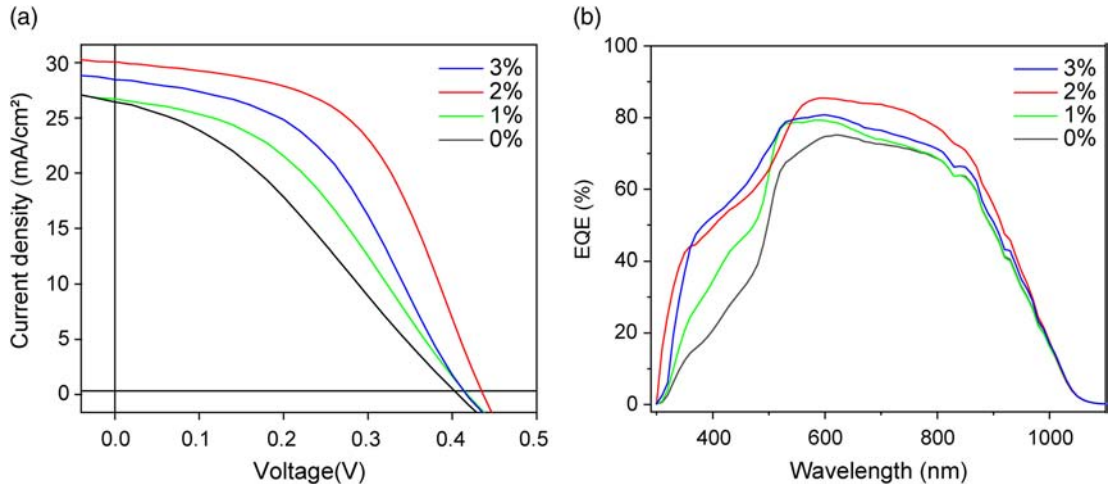

Figure 5. a) *J–V* curves, and b) EQE curves of FTO/CdS:O/Sb_2Se_3/graphite/Ag solar cells with sputtered oxygenated CdS:O window layers grown in the $O_2/Ar + O_2$ ratio at 0%, 1%, 2%, and 3% at ambient temperature.

Table 2. Device performance parameters of FTO/CdS:O/Sb_2Se_3/graphite/Ag solar cells with sputtered oxygenated CdS:O window layers grown in the $O_2/Ar+O_2$ ratio at 0%, 1%, 2%, and 3% at ambient temperature.

CdS:O	V_{OC} [V]	J_{SC} [mA cm^{-2}]	FF [%]	PCE [%]	R_S [Ω cm^2]	R_{SH} [Ω cm^2]
0%	0.402 ± 0.05	26.75 ± 0.5	33.27 ± 0.5	3.59 ± 0.2	163.58 ± 1	1077.55 ± 5
1%	0.419 ± 0.05	26.71 ± 0.5	40.34 ± 0.5	4.52 ± 0.2	146.86 ± 1	1535.97 ± 5
2%	0.432 ± 0.05	29.87 ± 0.5	54.00 ± 0.5	7.01 ± 0.2	71.26 ± 1	1916.95 ± 5
3%	0.424 ± 0.05	28.24 ± 0.5	46.32 ± 0.5	5.56 ± 0.2	117.12 ± 1	1423.92 ± 5

sputtered oxygenated CdS:O window layers, whereas the EQE response at long wavelength (>900 nm) remains unchanged. In addition to the gain at the short wavelength from the increased bandgap of CdS:O, the EQE response at shorter wavelength (e.g., from 500 to 900 nm) is also improved to 90% at 570 nm when oxygen partial pressure is increased from 0% to 2%, which can be attributed to the low recombination loss of photoexcited carriers (or long carrier diffusion length) in bulk Sb_2Se_3 with CdS:O sputtered at 2% oxygen partial pressure.

To ascertain the difference between the sputtered oxygenated CdS:O window layers and the conventional CBD deposited CdS window layer. We compare our sputtered CdS:O/Sb_2Se_3 champion devices with the best champion CBD CdS based Sb_2Se_3 devices deposited using the identical CSS conditions in our group. The sputtered CdS:O and CBD CdS films thickness is ≈60 nm. **Figure 6**a,b and **Table 3** show the *J–V* and EQE, and device parameters of the champion Sb_2Se_3 device using sputtered and CBD CdS window layer, respectively. Overall, the

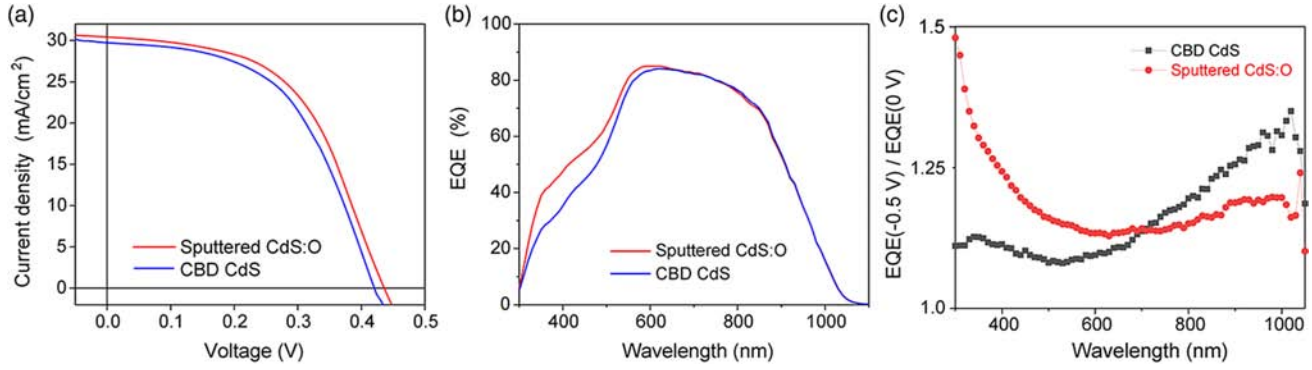

Figure 6. a) *J–V* curves, b) EQE (0 V) curves, and c) the ratio of EQE (−0.5 V)/EQE (0V) curves of the champion FTO/CdS:O/Sb_2Se_3/graphite/Ag solar cells with CBD-deposited CdS and sputtered oxygenated CdS:O window layers grown in the $O_2/Ar + O_2$ ratio at 2% at ambient temperature.

Table 3. Device performance parameters of FTO/CdS:O/Sb_2Se_3/graphite/Ag solar cells with sputtered oxygenated CdS:O window layers grown in the $O_2/Ar+O_2$ ratio at 2% at ambient temperature and CBD CdS.

CdS	V_{OC} [V]	J_{SC} [mA cm^{-2}]	FF [%]	PCE [%]	R_S [Ω cm^2]	R_{SH} [Ω cm^2]
Sputter CdS:O	0.432	29.87	54.00	7.01	71.26	1916.95
CBD CdS	0.414	29.11	50.80	6.12	64.02	1671.81

Sb_2Se_3 cells with sputtered CdS:O window layer outperform the Sb_2Se_3 devices with CBD CdS window layer, particularly in terms of the V_{OC} and FF. These device performance comparisons suggest a better diode behavior in the sputtered CdS:O/Sb_2Se_3 devices. The higher shunt resistance of sputtered CdS:O/Sb_2Se_3 devices also contributes to the improved FF, although the series resistivity is slightly higher than that of the Sb_2Se_3 device with CBD CdS window layer. The EQE spectra were also measured under bias voltage conditions (−0.5 V) and the ratio of EQE responses in the form of EQE (−0.5 V)/EQE (0 V), as shown in Figure 6c. An increase toward the longer wavelength was observed for the CBD CdS/Sb_2Se_3 devices, suggesting more collection of photocurrents at the rear side of Sb_2Se_3 with an internal electric field. However, the EQE ratio is approximately flat over the long wavelength (i.e., >600 nm) in the sputtered CdS:O/Sb_2Se_3 devices, indicating more photogenerated carriers without the assistance of internal electric field. Interestingly, for the short wavelength (<600 nm), the sputtered CdS:O window layer can collect more photogenerated carriers with the existence of an internal electric field than that of the CBD-deposited CdS, indicating that sputtered oxygenated CdS:O window layers are highly efficient for the carrier collection. Similar behavior was also observed with a solar cell capacitance simulator (SCAPS) device simulation, as shown in Figure S5, Supporting Information.

To characterize the microstructure origin of the improved device performance in CdS:O/Sb_2Se_3 solar cells, scanning electron microscopy (SEM) is used to analyze the surface morphology and crystallization of Sb_2Se_3 films. **Figure 7**a,b shows the top-view images of Sb_2Se_3 with CBD CdS and sputtered CdS:O (2%), respectively. The cross-sectional SEM image and energy dispersive spectroscopy (EDS) elemental mapping are shown in Figure 7c for the Sb_2Se_3 grown on sputtered CdS:O film (2%), suggesting that film thickness around 900 nm and the Sb/Se elements stabilize in the film. The grain size of the Sb_2Se_3 film grown on the sputtered CdS:O window layer is larger than that of the Sb_2Se_3 with the CBD CdS window layer, although the CSS growth conditions are identical. The grain-size distributions of the two SEM morphology images are shown in Figure 7d. The average grain size of Sb_2Se_3 with CBD CdS window layer is about 290 nm, whereas that of Sb_2Se_3 grown on sputtered CdS:O window layer is about 480 nm. The larger grain size of Sb_2Se_3 on the sputtered CdS:O window layer suggests that the grain-growth process is kinetically faster than that of Sb_2Se_3 on the CBD CdS. Moreover, the grain orientation prefers (211)-orientation in CdS:O/Sb_2Se_3, whereas the grain prefers (221)-orientation in CBD CdS/Sb_2Se_3 film (Figure S1, Supporting Information). The surface states of the Sb_2Se_3 grown on the sputtered CdS:O layer were characterized using the XPS. The Sb 3d and Se 3d spectra in Figure 7e,f indicate no clear trace of Sb_2O_3 and residual Se.

The local oxygen distribution at the interfacial area of these devices is investigated by secondary ion mass spectroscopy (SIMS) measurement. Figure 7g,h show the SIMS spectra of Sb, Se, Cd, S, and O in CBD CdS/Sb_2Se_3 and sputtered CdS:O/Sb_2Se_3 devices, respectively. Deeper Cd diffusion of ≈200 nm in CBD CdS/Sb_2Se_3 is observed, compared with that of ≈130 nm in the sputtered CdS:O/Sb_2Se_3 devices (Figure S4, Supporting Information). We may rule out the substrate temperature influence because it is identical during Sb_2Se_3 CSS deposition. However, the oxygen level is higher, and the Cd level is lower in Sb_2Se_3 with the sputtered CdS:O window layer than those with the CBD CdS window layer, confirming our theoretical results and suggesting that the oxygen from the CdS:O layer can suppress the Cd diffusion into Sb_2Se_3 at the junctions and prevent n-type buried homojunction located deep inside the Sb_2Se_3 absorber due to Cd interstitials.[26] Note that the oxygen in the sputtered oxygenated CdS:O window layer is in the SO_x^{2-} bonding environments, whereas the oxygen in the CBD CdS may be at trace level which is not incorporated with the Cd and S ions.[30] Thus, higher oxygen-concentration gradient at the interface of sputtered oxygentated CdS:O/Sb_2Se_3 will drive a deeper oxygen diffusion in the Sb_2Se_3 and block the Cd diffusion.

To better understand the mechanism of the improved device performance through the oxygenated interface in the CdS:O/Sb_2Se_3 devices compared with that of the CBD CdS/Sb_2Se_3 devices, we conducted the admittance spectroscopy, capacitance–voltage (*C*–*V*), and doping profiling characterization. **Figure 8**a shows the frequency dependence of the capacitance. The capacitance of the CdS:O/Sb_2Se_3 device is less frequency-dependent than that of CBD CdS/Sb_2Se_3, suggesting a reduced trap density in CdS:O/Sb_2Se_3 device. The Mott–Schottky analysis as shown in Figure 8c is performed by analyzing the *C*–*V* profile under dark at room temperature based on $\frac{1}{C^2} = \frac{2}{q\varepsilon_0\varepsilon A^2 N}(V_{bi} - V)$, where *C* is capacitance, *q* is the electronic charge, *A* is device area, ε_0 is the permittivity of vacuum, ε is the relative dielectric constant of Sb_2Se_3, *N* is carrier concentration, and V_{bi} is the built-in potential. The V_{bi} of the Sb_2Se_3 solar cells can be determined through the $1/C^2$-Voltage curve as shown in Figure 8b. The voltage intercept is 0.52 and 0.41 V for sputtered oxygenated CdS:O and CBD CdS buffered Sb_2Se_3, respectively, indicating increased built-in electric field in CdS:O/Sb_2Se_3 devices. Thus, the increased V_{bi} can reduce photogenerated charge accumulation at the interfacial area and lead to improved V_{OC} in CdS:O/Sb_2Se_3 devices. Figure 8c shows the *C*–*V* doping profiles for both sputtered CdS:O/Sb_2Se_3 and CBD CdS/Sb_2Se_3 devices, which provide insights about the interfacial area defects. The *C*–*V* doping density in CBD CdS/Sb_2Se_3 devices is $\approx 2.35 \times 10^{16}$ cm^{-3}, and the corresponding depletion width is ≈207 nm. Importantly, for the sputtered CdS:O/Sb_2Se_3, the doping density slightly decreases to 2.08×10^{16} cm^{-3}, and the depletion width is extended to 265 nm. A broader depletion zone (i.e., a decrease of capacitance) could collect more photogenerated carrier and contribute to larger photocurrent (J_{SC}). The reduced carrier doping density in the sputtered CdS:O/Sb_2Se_3 may originate from the depletion region mainly located at the CdS:O/Sb_2Se_3 interface. The interfacial defect density is estimated to be 4.86×10^{12} and 5.51×10^{12} cm^{-2} for CBD CdS/Sb_2Se_3 and sputtered CdS:O/Sb_2Se_3 devices, respectively, suggesting that the

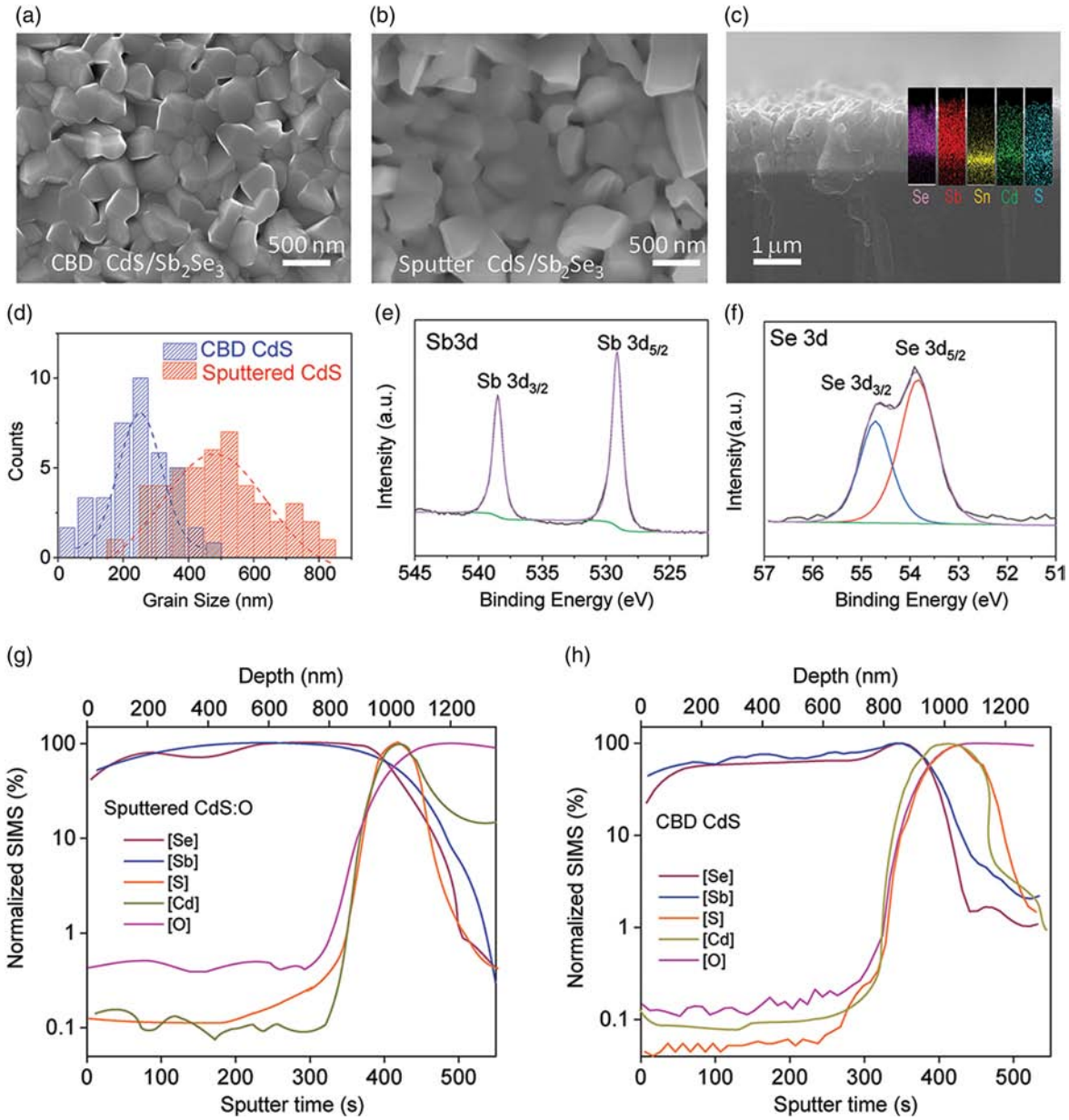

Figure 7. a,b) Top view of the SEM images with EDS spectra in the inset of Sb_2Se_3 with the CBD-deposited CdS and sputtered oxygenated CdS:O window layer, respectively; c) cross-sectional SEM images of the oxygenated CdS:O buffered Sb_2Se_3 with EDS mapping for the selected area; d) histogram distribution of grain size for CBD and sputtered oxygenated CdS buffered Sb_2Se_3 film; e,f) XPS data for the Sb3d and Se3d in the oxygenated CdS/Sb_2Se_3 film; and g,h) SIMS spectra for the sputtered oxygenated and CBD CdS based Sb_2Se_3 devices, respectively.

sputtered CdS:O/Sb_2Se_3 interface has more active defects contributing to the improved device performance. Figure 8d shows the Nyquist plots characterized by electrochemical impedance spectroscopy (EIS) to elucidate the interfacial charge transport kinetics in the devices. The internal series resistance (R_S) is 29.19 and 21.28 Ω and the recombination resistance (R_{rec}) is 821.4 and 1059 Ω for CdS:O/Sb_2Se_3 and sputtered CdS:O/Sb_2Se_3 devices, respectively, indicating that the carrier accumulation and recombination are weak in the sputtered CdS:O/Sb_2Se_3 devices. Thus, in terms of the interfacial charge transport behavior, we may conclude that the sputtered CdS:O windows layer could provide a wider-depletion region in Sb_2Se_3 absorber layer to collect more photogenerated carrier. Moreover, the sputtered CdS:O/Sb_2Se_3 device also exhibits a higher built-in voltage and lower recombination interface, which contribute to the increased V_{OC} and J_{SC}.

3. Conclusions

In summary, through a combined theoretical and experimental study, we have demonstrated an effective interface engineering

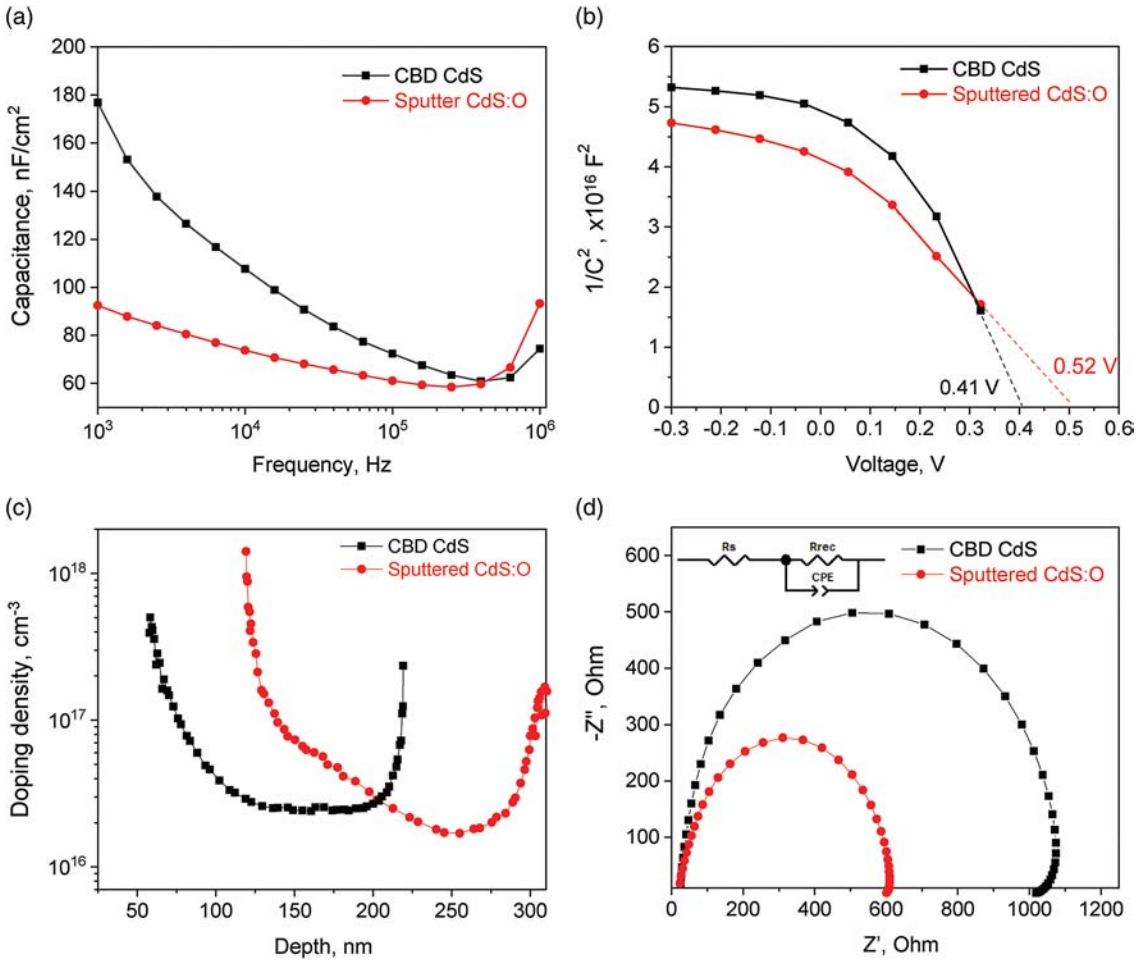

Figure 8. a) Frequency dependence of the capacitance (*C*); b) $1/C^2$ versus applied voltage (*V*) graphs; c) logarithmic representation of a *C–V* derived carrier density profiles; and d) Nyquist plots for the sputtered oxygenated CdS:O and CBD CdS based Sb_2Se_3 devices, respectively.

approach to increase the Sb_2Se_3 photovoltaic device performance by using sputtered oxygenated CdS (CdS:O) as a window layer by replacing the conventional CBD-deposited CdS window layer. The open-circuit voltage, photocurrent, and fill factor are all improved with the best PCE of ≈7.01% (V_{OC} of 0.432 V, FF of 54%, and J_{SC} of ≈29.87 mA cm^{-2}) in the CdS:O/Sb_2Se_3 device. The benefit of the sputtered oxygenated CdS:O window layer for the Sb_2Se_3 devices originates from the improved bandgap of CdS:O with high resistivity of $CdSO_x$, and transmittance that allows more light absorption in the Sb_2Se_3 absorber. Meanwhile, both theoretical calculations and experimental results show that the sputtered oxygenated CdS:O window layer can prevent the formation of Cd interstitial defects in the Sb_2Se_3 layer due to the accumulation of the oxygen at the interface between CdS:O and Sb_2Se_3 layers. Our work suggests that the optimization of the window layer can greatly improve the open-circuit voltage and enhance the device performance of the emerging antimony chalcogenide Sb_2Se_3 and Sb_2S_3 thin-film solar cells.

4. Experimental Section

Films Deposition and Characterization: The sputtered pure CdS and oxygenated CdS (CdS:O) window layers were deposited by radio frequency (RF) sputtering system (AJA ATC Orion 5) of a CdS target (2-in. in diameter) at ambient temperature. The base pressure for the sputtering was pumped down to 7×10^{-8} Torr. The oxygenated CdS:O layers were reactively sputtered in a mixture gas (≈5 mTorr) between O_2 and Ar gas (99.999% purity, Airgas, USA) at a total flow rate of 20 sccm. The oxygen partial pressure (O_2/Ar + O_2) was controlled using the O_2 and Ar mass flow to 0%, 1%, 2%, and 3%, respectively. Oxygenated CdS:O films were deposited on F:SnO_2-coated soda lime glass (FTO, NSG, USA) with a thickness around 80 nm via controlling the deposition time and power. As a comparison, the CBD CdS was also fabricated on the FTO glass. The Sb_2Se_3 films with thickness ≈1 µm were grown by CSS, as reported by Guo et al.[8] The Sb_2Se_3 film deposition used a source and substrate temperature at 550 and 300 °C, respectively, and the deposition pressure was about 10 mTorr. The optical properties for the CdS and Sb_2Se_3 films were characterized using the UV–vis spectrometer (Shimadzu UV-1800). The crystalline structure of CdS:O and Sb_2Se_3 film were characterized by XRD with Cu Kα radiation (Philips X'Pert). Surface morphology of CdS:O was investigated by atomic force microscopy (AFM; Park XE70) and a scanning

electron microscopy (SEM; JOEL 7000). The chemical composition was determined by the energy dispersive spectroscopy (EDS) attached to the SEM. XPS was collected using the Kratos Axis 165 XPS with Al source.

Solar Cell Fabrication and Characterization: The Sb_2Se_3 film solar cells with the sputtered oxygenated CdS:O windows layer were fabricated with conventional superstrate device structure: glass/FTO/CdS:O/Sb_2Se_3/Graphite/Ag. Graphite back contact was screen printed onto films followed by Ag deposition by sputtering. The cells area was ≈0.08 cm^2. The current density–voltage (*J–V*) curves of the CdS:O/Sb_2Se_3 devices were measured by the Newport Sol3A class AAA solar simulator (Oriel, model 94023A, Newport Corporation, Irvine, CA, USA) under ambient conditions (room temperature, 1000 W m^{-1}, AM 1.5 G illumination). A Keithley 2420 SourceMeter (Keithley Instrument Inc.) was used to acquire *J–V* characteristics. EQE of solar cells was measured with a commercial solar cell spectral-response measurement system (QE-T, Enli Technology, Co. Ltd). Capacitance–Voltage (*C–V*) measurement was performed in dark at room temperature using a Solartron Analytical 1260 impedance analyzer equipped with a 1296 dielectric interface at a frequency of 10 kHz, and the AC amplitude was 50 mV. DC bias was changed from −0.3 to 0.3 V. EIS measurements were carried out using Solartron Analytical 1260 impedance analyzer at a bias potential of 0.5 V in dark with the frequency range of 10^2–10^6 Hz.

First-Principles Electronic Structure Calculations: Cd and O diffusion energy barriers in Sb_2Se_3 were calculated using the climbed image nudged elastic band (NEB) method.[31] The total energy calculations were based on first-principles DFT[32,33] as implemented in the Vienna Ab initio Simulation Package (VASP).[34] The Perdew–Burke–Ernzerhof (PBE)[35] form of exchange-correlation functional within the generalized gradient approximation (GGA)[36] and a plane wave basis set with a 400 eV energy cutoff were used in the DFT calculations. The structural optimization of bulk Sb_2Se_3 was performed with a Γ-centered Monkhorst-Pack k-point sampling grid of $4 \times 4 \times 12$, a maximal residual force of less than 0.01 eV $Å^{-1}$,[37] and an energy convergence criterion of 10^{-6} eV for electronic relaxation. The optB86-vdW nonlocal correlation functional was adopted to account for the weak vdW interactions between ribbons.[38–40] The calculated lattice parameters *a*, *b*, and *c* of the unit cell are 11.482, 11.870, and 4.014 Å, respectively. A supercell of $1 \times 1 \times 3$ was constructed to determine the diffusion energy barrier in the dilute limit.

First-Principles Calculations of Point Defects in Sb_2Se_3: For defect formation energy and transition levels, we used the finite-size correction scheme proposed by Freysoldt et al.[41] and Oba and co-workers.[42] The unit cell structure was enlarged to $2 \times 2 \times 6$ supercell, containing 480 atoms, to minimize the errors caused by image charge interaction. The charged defect formation energy is defined by $\Delta E^f = E(D,q) - E(\text{bulk}) - \sum n_i\mu_i + q\epsilon_F + E_{corr}$. Here *E(D, q)* is the total energy of the defect supercell with charge *q*, and $E(\text{bulk})$ is the total energy of pristine cell without any defect. μ_i *i* involved in the defect, and n_i corresponds to the number of atoms added ($n_i < 0$) or removed ($n_i < 0$). ϵ_F is the Fermi level using the VBM as the reference. E_{corr} refers to the correction term. It mainly consists of two parts: the electrostatic potential alignment between the defect cell and the bulk, and the interaction between the charge and its images due to the periodic boundary condition used in the DFT calculations.

Supporting Information

Supporting Information is available from the Wiley Online Library or from the author.

Acknowledgements

L.G. and B.Z. contributed equally to this work. L.G. and F.Y. acknowledge the support from the resources of Alabama Water Institute at The University of Alabama and National Science Foundation under Grant No. 1844210. X.Q. gratefully acknowledges partial support of NSF under Award Number DMR-1753054. The authors also acknowledge Dr. Stanislav Verkhoturov of Materials Characterization Facility (MCF) at Texas A&M University for his assistance in SIMS.

Conflict of Interest

The authors declare no conflict of interest.

Keywords

first-principles calculations, interdiffusion, interface engineering, Sb_2Se_3 thin-film solar cells, sputtered oxygenated CdS

Received: May 18, 2019
Revised: June 13, 2019
Published online:

[1] M. A. Green, S. P. Bremner, *Nat. Mater.* **2017**, *16*, 23.
[2] Y. Zhou, L. Wang, S. Y. Chen, S. K. Qin, X. S. Liu, J. Chen, D. J. Xue, M. Luo, Y. Z. Cao, Y. B. Cheng, E. H. Sargent, J. Tang, *Nat. Photon.* **2015**, *9*, 409.
[3] X. Wen, C. Chen, S. Lu, K. Li, R. Kondrotas, Y. Zhao, W. Chen, L. Gao, C. Wang, J. Zhang, G. Niu, J. Tang, *Nat. Commun.* **2018**, *9*, 2179.
[4] L. Wang, D.-B. Li, K. Li, C. Chen, H.-X. Deng, L. Gao, Y. Zhao, F. Jiang, L. Li, F. Huang, Y. He, H. Song, G. Niu, J. Tang, *Nat. Energy* **2017**, *2*, 17046.
[5] K. Zeng, D. J. Xue, J. Tang, *Semicond. Sci. Tech.* **2016**, *31*, 063001.
[6] Z. Li, X. Liang, G. Li, H. Liu, H. Zhang, J. Guo, J. Chen, K. Shen, X. San, W. Yu, R. E. I. Schropp, Y. Mai, *Nat. Commun.* **2019**, *10*, 125.
[7] D.-B. Li, X. Yin, C. R. Grice, L. Guan, Z. Song, C. Wang, C. Chen, K. Li, A. J. Cimaroli, R. A. Awni, *Nano Energy* **2018**, *49*, 346.
[8] L. Guo, B. Zhang, Y. Qin, D. Li, L. Li, X. Qian, F. Yan, *Sol. RRL* **2018**, *2*, 1800128.
[9] C. Yuan, L. Zhang, W. Liu, C. Zhu, *Sol. Energy* **2016**, *137*, 256.
[10] X. X. Wen, Y. S. He, C. Chen, X. S. Liu, L. Wang, B. Yang, M. Y. Leng, H. B. Song, K. Zeng, D. B. Li, K. H. Li, L. Gao, J. Tang, *Sol. Energy Mater. Sol. C* **2017**, *172*, 74.
[11] X. Liu, C. Chen, L. Wang, J. Zhong, M. Luo, J. Chen, D. J. Xue, D. Li, Y. Zhou, J. Tang, *Prog. Photovoltaic Res. Appl.* **2015**, *23*, 1828.
[12] S. Messina, M. T. S. Nair, P. K. Nair, *J. Electrochem. Soc.* **2009**, *156*, H327.
[13] C. Chen, Y. Zhao, S. C. Lu, K. H. Li, Y. Li, B. Yang, W. H. Chen, L. Wang, D. B. Li, H. Deng, F. Yi, J. Tang, *Adv. Energy Mater.* **2017**, *7*, 1700866.
[14] L. Wang, M. Luo, S. Qin, X. Liu, J. Chen, B. Yang, M. Leng, D.-J. Xue, Y. Zhou, L. Gao, *Appl. Phys. Lett.* **2015**, *107*, 143902.
[15] M. Huang, P. Xu, D. Han, J. Tang, S. Chen, *ACS Appl. Mater. Interfaces* **2019**, *11*, 15564.
[16] L.-Y. Lin, L.-Q. Jiang, Y. Qiu, B.-D. Fan, *J. Phys. Chem. Solids* **2018**, *122*, 19.
[17] M. A. Green, Y. Hishikawa, E. D. Dunlop, D. H. Levi, J. Hohl-Ebinger, A. W. Y. Ho-Baillie, *Prog. Photovoltaic Res. Appl.* **2018**, *26*, 427.
[18] A. Gupta, K. Allada, S. H. Lee, A. D. Compaan, *MRS Proc.* **2003**, *763*, B8.9.
[19] D. M. Meysing, C. A. Wolden, M. M. Griffith, H. Mahabaduge, J. Pankow, M. O. Reese, J. M. Burst, W. L. Rance, T. M. Barnes, *J. Vac. Sci. Technol., A* **2015**, *33*, 021203.
[20] J. Ge, P. Koirala, C. R. Grice, P. J. Roland, Y. Yu, X. X. Tan, R. J. Ellingson, R. W. Collins, Y. F. Yan, *Adv. Energy Mater.* **2017**, *7*, 1601803.

[21] J. M. Kephart, R. Geisthardt, W. S. Sampath, in 38th IEEE Photovoltaic Specialists Conf., IEEE **2012**, 854.
[22] N. R. Paudel, J. D. Poplawsky, K. L. Moore, Y. Yan, *IEEE J. Photovoltaic* **2015**, *5*, 1492.
[23] Y. Yan, D. Albin, M. M. Al-Jassim, *Appl. Phys. Lett.* **2001**, *78*, 171.
[24] D. H. Rose, D. H. Levi, R. J. Matson, D. S. Albin, R. G. Dhere, P. Sheldon, in Conf. on IEEE Photovoltaic Specialists Conf. **1996**, 777.
[25] X. Liu, X. Xiao, Y. Yang, D.-J. Xue, D.-B. Li, C. Chen, S. Lu, L. Gao, Y. He, M. C. Beard, G. Wang, S. Chen, J. Tang, *Prog. Photovoltaic Res. Appl.* **2017**, *25*, 861.
[26] Y. Zhou, Y. Li, J. J. Luo, D. B. Li, X. S. Liu, C. Chen, H. B. Song, J. Y. Ma, D. J. Xue, B. Yang, J. Tang, *Appl. Phys. Lett.* **2017**, *111*, 013901.
[27] W. Wang, X. Wang, G. Chen, B. Chen, H. Cai, T. Chen, S. Chen, Z. Huang, C. Zhu, Y. Zhang, *Sol. RRL* **2018**, *2*, 1800208.
[28] D. A. Duncan, J. M. Kephart, K. Horsley, M. Blum, M. Mezher, L. Weinhardt, M. Haming, R. G. Wilks, T. Hofmann, W. L. Yang, M. Bar, W. S. Sampath, C. Heske, *ACS Appl. Mater. Interfaces* **2015**, *7*, 16382.
[29] N. R. Paudel, Y. F. Yan, *Appl. Phys. Lett.* **2014**, *105*, 183510.
[30] F. Lisco, P. M. Kaminski, A. Abbas, K. Bass, J. W. Bowers, G. Claudio, M. Losurdo, J. M. Walls, *Thin Solid Films* **2015**, *582*, 323.
[31] G. Henkelman, B. P. Uberuaga, H. Jónsson, *J. Chem. Phys.* **2000**, *113*, 9901.
[32] P. Hohenberg, W. Kohn, *Phys. Rev.* **1964**, *136*, B864.
[33] W. Kohn, L. J. Sham, *Phys. Rev.* **1965**, *140*, 1133.
[34] G. Kresse, J. Furthmüller, *Phys. Rev. B* **1996**, *54*, 11169.
[35] J. P. Perdew, K. Burke, M. Ernzerhof, *Phys. Rev. Lett.* **1996**, *77*, 3865.
[36] D. C. Langreth, M. J. Mehl, *Phys. Rev. B* **1983**, *28*, 1809.
[37] H. J. Monkhorst, J. D. Pack, *Phys. Rev. B* **1976**, *13*, 5188.
[38] M. Dion, H. Rydberg, E. Schröder, D. C. Langreth, B. I. Lundqvist, *Phys. Rev. Lett.* **2004**, *92*, 246401.
[39] G. Román-Pérez, J. M. Soler, *Phys. Rev. Lett.* **2009**, *103*, 096102.
[40] J. Klimeš, D. R. Bowler, A. Michaelides, *Phys. Rev. B* **2011**, *83*, 195131.
[41] C. Freysoldt, J. Neugebauer, C. G. Van de Walle, *Phys. Rev. Lett.* **2009**, *102*, 016402.
[42] Y. Kumagai, F. Oba, *Phys. Rev. B* **2014**, *89*, 195205.